

Article

Synthesis of Carbon Nanotubes by Plasma-Enhanced Chemical Vapor Deposition Using $\text{Fe}_{1-x}\text{Mn}_x\text{O}$ Nanoparticles as Catalysts: How Does the Catalytic Activity of Graphitization Affect the Yields and Morphology?

Takashi Yanase , Takuya Miura, Tatsuya Shiratori, Mengting Weng, Taro Nagahama and Toshihiro Shimada 

Division of Applied Chemistry, Faculty of Engineering, Hokkaido University, Kita 13 Nishi 8 Kita-ku, Sapporo 060-8628, Japan

* Correspondence: yanase42@eng.hokudai.ac.jp; Tel.: +011-706-6571

Received: 26 June 2019; Accepted: 6 August 2019; Published: 8 August 2019



Abstract: The choice of a catalyst for carbon nanotube (CNT) growth is critical to controlling the morphology and chirality of the final product. Plasma-enhanced chemical vapor deposition (PECVD) can alleviate the requirements of the catalyst, i.e., they must be active for both the decomposition of the source gas and graphitization in the conventional thermal CVD. However, it is still not well understood how the catalytic activity of the graphitization affects the yield and quality of CNTs. In this paper, we systematically investigated the influence of the catalytic activity of graphitization by tuning the composition of $\text{Fe}_{1-x}\text{Mn}_x\text{O}$ ($x = 0-1$) nanoparticles as catalysts. As the Mn component increased, the number of CNTs decreased because Mn has no catalytic function of the graphitization. The quality of CNTs also affected by the inclusion of the Mn component. Our study may provide useful information to develop a new catalyst for CNT growth in PECVD.

Keywords: carbon nanotube; plasma-enhanced chemical vapor deposition; $\text{Fe}_{1-x}\text{Mn}_x\text{O}$ nanoparticle

1. Introduction

The carbon nanotube (CNT) has been widely studied since its discovery [1,2] due to its excellent properties such as high thermal conductivity [3], toughness [4] and high carrier mobility [5–9]. Several kinds of synthetic methods have been established to grow the CNTs, for instance, arc discharge [10,11], laser ablation [12] and thermal chemical vapor deposition (CVD) [13–21]. The thermal CVD is currently the most widely used technique for the CNT production due to its high yield, high quality and ease of use. Two primary methods of HiPCO [22] and super-growth [23] were invented by Nikolaev et al. and Hata et al., respectively, for the mass production of the single-walled CNT (SWCNT). After the invention of these two methods, many researchers tried to synthesize SWCNTs with single chirality for over ten years because the chirality determines the electronic property of the SWCNT. (6, 5) SWCNTs with chirality in a proportion higher than 50% were produced using the CoMo catalyst supported by porous silica [14,24]. When using the FeRu catalyst, the chirality depends on the reaction temperature; (6, 5) SWCNTs and a mixture of (8, 4) and (7, 5) SWCNTs are synthesized at 600 °C and 850 °C, respectively [15]. In 2014, (6, 6) SWCNTs were grown using singly capped ultrashort SWCNTs that were synthesized via barrel-shaped organic molecules ($\text{C}_{96}\text{H}_{54}$) [25]. A single chirality (12, 6) in a proportion more significant than 92% was achieved for the SWCNT growth using the W-Co nanocrystal catalyst [26]. For further improvement of the quality of CNT, many researchers are still intensively

exploring the catalysts for the SWCNT growth because the SWCNT growth with a higher selectivity is desirable for electronic applications.

However, searching for a new catalyst is very challenging due to the strict requirements for the catalyst for the thermal CVD, which must possess both functions of decomposition of the source gas and graphitization of the carbon species [27–30]. The plasma-enhanced CVD (PECVD) can alleviate such strict requirements for the CNT growth because a high energy plasma makes active carbon species. Another advantage of the PECVD is that the amount of supplied ionized carbon species onto the surface of the catalyst can be tuned by applying a voltage to the substrate. Kato et al. demonstrated that the chirality distribution and growth rate of the SWCNTs in the PECVD could be controlled by tuning the size of the nanoparticles (catalysts) and the flow rate of H₂ [31,32]. Although many articles reported the low-temperature synthesis of CNTs, synthesis of free-standing CNTs and synthesis of horizontally aligned CNTs by PECVD [33–36], it is still not well studied how the catalytic activity of the graphitization influences the yield and morphology of CNTs.

The purpose of this study is to systematically investigate how catalytic activity affects the yield and morphology of CNTs, which must be well understood before searching for a new catalyst for the CNT growth. In order to achieve this purpose, Fe_{1-x}Mn_xO ($x = 0-1$) was selected as a catalytic nanoparticle because it is well-known that Fe is a suitable catalyst in the thermal CVD while Mn is not. Furthermore, it is easy to tune the chemical composition, which is x by controlling the synthetic conditions. Our study may provide useful information to develop a new catalyst for CNT growth.

2. Materials and Methods

The Fe_{1-x}Mn_xO nanoparticles that were synthesized according to Hou [37] were used for the catalyst of the CNT growth. It was confirmed that the same procedure to make FeO nanoparticles can be used for the synthesis of the Fe_{1-x}Mn_xO nanoparticles if the corresponding ratio of the acetylacetonate complexes (starting materials) is used except when $x = 1$ (pristine MnO). We found that the MnO particles synthesized following the same procedure as Hou reported [37] were large (~200 nm). Therefore, the hot injection method [38,39] was used for preparing the MnO nanoparticles. The ratio of the acetylacetonate complexes in the source materials is summarized in Table 1.

Table 1. The ratio of acetylacetonate complex in the source materials to prepare Fe_{1-x}Mn_xO nanoparticles was shown in the first and second rows. acac stands for acetylacetonate. The volumes of oleylamine and oleic acid (solvents) are both 5 mL. Chemical compositions evaluated by energy-dispersive X-ray spectroscopy and X-ray diffraction were shown in the third row and fourth row, respectively.

	Fe(acac) ₃ /mmol	Mn(acac) ₃ /mmol	x by EDS	x by XRD
(i)	2.0	0	0	0
(ii)	1.0	1.0	0.5	0.5
(iii)	0.17	1.8	0.97	0.9
(iv)	0	2.0	1	1

We found that FeO nanoparticles were reduced into Fe nanoparticles during PECVD by the active species generated in the plasma, which was confirmed by acquiring an electron diffraction pattern of the nanoparticles after the PECVD as shown in Figure 1. The inset shows a transmission electron microscope (TEM, JEM-2010, JEOL, Tokyo, Japan) image of the Fe nanoparticles attached to the CNTs. We further confirmed with a scanning electron microscope (SEM, JSM-6500F, JEOL, Tokyo, Japan) that there was no significant difference in the CNT growth in both cases when we used FeO nanoparticles with and without hydrogen treatment as shown in Figure 2a,b. Therefore, we did not carry out any special treatment, such as hydrogen treatment to reduce FeO into Fe in this study.

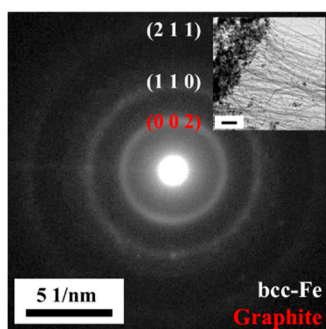


Figure 1. An electron diffraction pattern of the Fe nanoparticles after Plasma-enhanced chemical vapor deposition (PECVD). Inset shows the TEM image of nanoparticles attached to the carbon nanotubes (CNTs). Scale bar in the inset shows 100 nm.

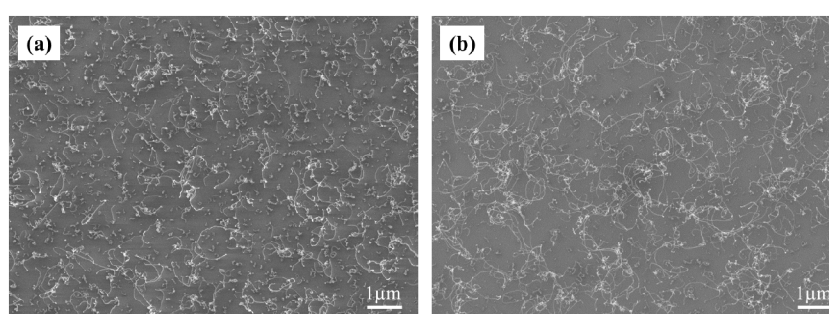


Figure 2. The surface morphology after the CNT growth with (a) and without (b) hydrogen treatment.

The specially designed PECVD chamber that can directly monitor the temperature under a high bias voltage using a thermocouple was utilized in this study. The detailed geometry of the PECVD chamber was described in the previous report [40]. A SiO₂(285 nm)/Si wafer was cut into several 1 × 1 cm² pieces and cleaned by the RCA method [41], then an Al₂O₃ layer was deposited by sputtering, if necessary. The oxide nanoparticles dispersed in a hexane solution were dip-coated on the substrate in a glove box. The substrates were transferred to the chamber as quickly as possible because the monoxide nanoparticles are gradually oxidized in air. After the substrates were introduced into the PECVD chamber, then the chamber was evacuated. When the pressure reached 1 × 10⁻⁴ Pa, the substrate was heated to 650 °C, then methane (CH₄) was introduced into the chamber. The pressure was adjusted to 70 Pa that is the optimal pressure to form a stable plasma. The radiofrequency plasma was turned on, and the power was fixed at 20 W. A bias voltage (−200 V) was applied to the substrate, and the shutter was opened to start the PECVD. After a 10 min reaction, the shutter was closed to stop the growth of the CNTs. The plasma and the heater were turned off to avoid any undesired reaction while cooling.

XRD (Rint Ultima 2000, Rigaku, Tokyo, Japan) was measured to identify the nanoparticles with Cu Kα radiation ($\lambda = 0.154056$ nm). A TEM (JEM-2010, JEOL, Tokyo, Japan) and an SEM (JSM-6500F, JEOL, Tokyo, Japan) were used to observe the morphology of the nanoparticles and CNTs. An energy dispersive X-ray spectrometer (EDS) attached to the TEM was used to conduct the elemental analysis. The structural order of the CNTs was analyzed by Raman spectroscopy (Renishaw Invia) with a 532 nm excitation laser.

3. Results and Discussion

The dispersity of the nanoparticles on a substrate is very important to make dense CNTs [42,43]. Hence we examined the dispersity on the six kinds of substrate: SiO₂/Si(100), SiO₂/Si(100) with scratches, Si(100), 7° off Si(100), a molybdenum plate and Al₂O₃/SiO₂/Si. Only the Al₂O₃/SiO₂/Si substrate was effective to uniformly disperse the FeO nanoparticles as shown in Figure 3a. The FeO

nanoparticles on a SiO₂/Si substrate aggregated, forming large clusters as seen in Figure 3b. Such aggregation also occurred when using the other four substrates (not shown). The dispersity of Fe nanoparticles on the Al₂O₃/SiO₂/Si substrate was maintained even though the substrate was heated to 650 °C. To demonstrate how the Al₂O₃ layer influences a final product, the PECVD was carried out for the substrates with and without the Al₂O₃ layer. The density of CNT synthesized with the Al₂O₃ layer (Figure 4a) was much higher than that without the Al₂O₃ (Figure 4b) because the aggregation lowered the activity of the nanoparticles. This result clearly illustrates that the Al₂O₃ layer is useful for suppressing the aggregation of the FeO nanoparticles and for the dense CNT growth. The suppression of the aggregation can be explained by the rough surface of the Al₂O₃ layer, which prevents the particles from moving on the surface. It is noteworthy that the Al₂O₃ does not show the catalytic function for the CNT growth because nothing formed when the Al₂O₃/SiO₂/Si substrates without FeO nanoparticles were used. This result also indicates that only the function of graphitization is required in PECVD because no CNT grew at 650 °C and the CNT growth was observed at above 800 °C when the conventional thermal CVD was carried out.

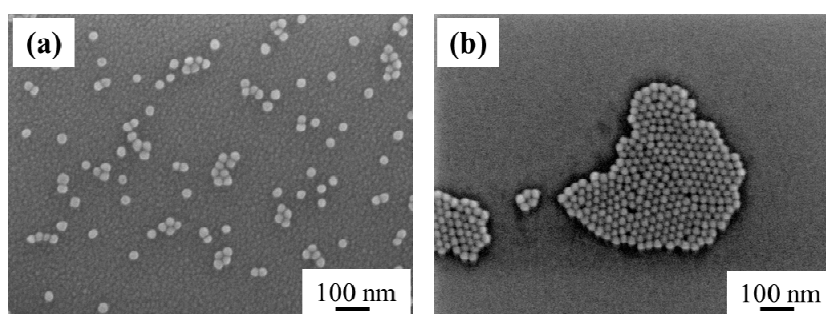


Figure 3. Dispersity of the FeO nanoparticles on (a) an Al₂O₃/SiO₂/Si substrate and (b) a SiO₂/Si substrate.

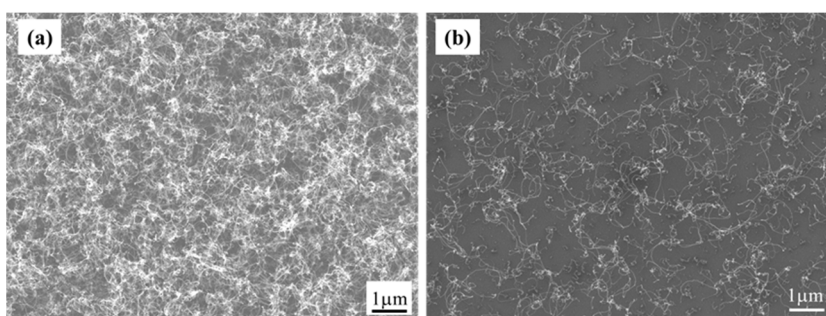


Figure 4. The surface morphology after the CNT growth (a) with Al₂O₃ layer and (b) without Al₂O₃ layer.

Figure 5 shows TEM images of four kinds of nanoparticles prepared as mentioned in the Experimental section. Since we focus on the catalytic function of the graphitization of nanoparticles, minor differences in the size and shape of nanoparticles can be ignored. The exclusion of the size and shape effects was justified by [44–47] those reported that multi-walled carbon nanotube (MWCNT) could be synthesized using nanoparticles with any shape when the size is smaller than ~100 nm. Therefore, the catalytic activities of Fe_{1-x}Mn_xO particles were examined merely by tuning the composition ratio of the nanoparticles. The Mn ratios (x) were evaluated by TEM-EDS as x = 0.5 and 0.97 for (ii) and (iii), respectively (see Table 1). XRD patterns of four nanoparticles were obtained to identify the nanoparticles and to evaluate the compositional uniformity of the alloy as shown in Figure 6a. All nanoparticles were identified as fcc-structure monoxides from (111), (200), (220), (311), and (222) peaks. The shoulder peak at 34.5° for the pristine FeO is due to the surface oxidation of the FeO nanoparticles while acquiring the XRD pattern. Similar air oxidation was also observed in the

previous study [37]. No peak splitting indicates that Fe and Mn were uniformly distributed in the $\text{Fe}_{1-x}\text{Mn}_x\text{O}$ nanoparticles. The (200) peaks were extracted to see the peak shift in Figure 6b clearly. The minimum variation of the peak shift is larger than the angular resolution, and the chemical composition can be calculated based on Vegard's law that is formulated as follows

$$a_{\text{Fe}_{1-x}\text{Mn}_x\text{O}} = (1-x)a_{\text{FeO}} + xa_{\text{MnO}},$$

where $a_{\text{Fe}_{1-x}\text{Mn}_x\text{O}}$ is the lattice constant of $\text{Fe}_{1-x}\text{Mn}_x\text{O}$, a_{FeO} is one of the pristine FeO (0.2139 nm) and a_{MnO} is one of the pristine MnO (0.2223 nm). The Mn ratios (x) of (ii) and (iii) were calculated as 0.5 and 0.9, respectively. These results are consistent with the chemical compositions evaluated by TEM-EDS analysis. It is concluded that the chemical composition of $\text{Fe}_{1-x}\text{Mn}_x\text{O}$ nanoparticles can be controlled by adjusting the ratio of the acetylacetonate complexes in the source materials. The x estimated by both TEM-EDS and XRD are summarized in Table 1.

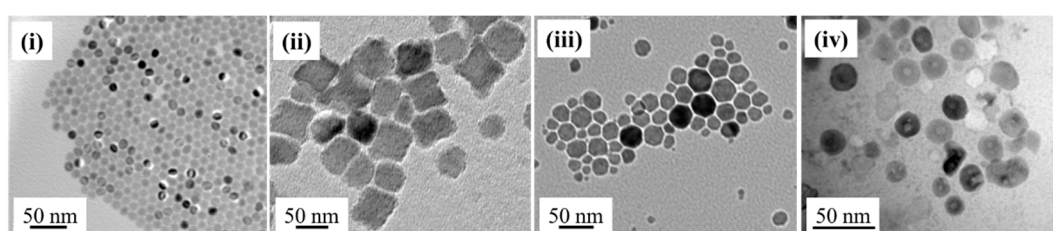


Figure 5. TEM images of the $\text{Fe}_{1-x}\text{Mn}_x\text{O}$ nanoparticles with different composition ratio. (i–iv) are as indicated in Table 1 that corresponds to different x in composition.

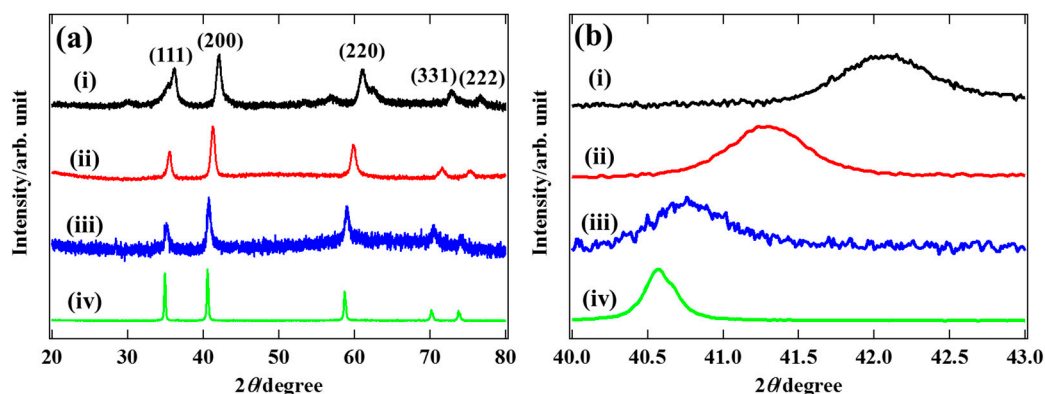


Figure 6. (a) XRD patterns of nanoparticles. (b) Enlarged (200) peak to show the peak shift. (i)–(iv) are as indicated in Table 1.

Figure 7 shows the surface morphologies of the substrates after the PECVD was carried out for all nanoparticles. The density of CNT decreased as Fe ratio decreased, then finally, nothing formed when the pristine MnO nanoparticles were used. The number density of CNT was roughly estimated from SEM images as $48 \mu\text{m}^{-2}$ for (i), $24 \mu\text{m}^{-2}$ for (ii) and $4 \mu\text{m}^{-2}$ for (iii). This result shows that the number of catalytic sites of graphitization decreased as the Mn ratio increased, which means that the catalytic activity of graphitization can be tuned by adjusting the composition ratio. It should be noted that the possibility of the existence of pure FeO nanoparticles in samples (ii) and (iii) is not likely considering the XRD result (Figure 6) that shows no phase separation. Samples (i) and (ii) were scrutinized by TEM and Raman spectroscopy to clarify the quality of the CNTs.

Figure 8a,b show the TEM image and the electron diffraction pattern of the CNTs for samples (i) and (ii). The tubular structure was seen for both samples, and most of the nanotubes were MWCNTs. The average number of graphene layers on the wall was calculated as 12 by assuming the interlayer distance of graphite (0.336 nm). The electron diffraction analysis shows the ring pattern attributed to the graphitic layered structure of (002) plane, which is from the side walls parallel to the direction

of the electron beam [2,48]. The average diameters of the samples (i) and (ii) were estimated from Figure 8 as 18 ± 13 nm and 29 ± 14 nm, respectively. We concluded from this result that the diameter of the CNT was determined by the size of nanoparticles, not the chemical composition.

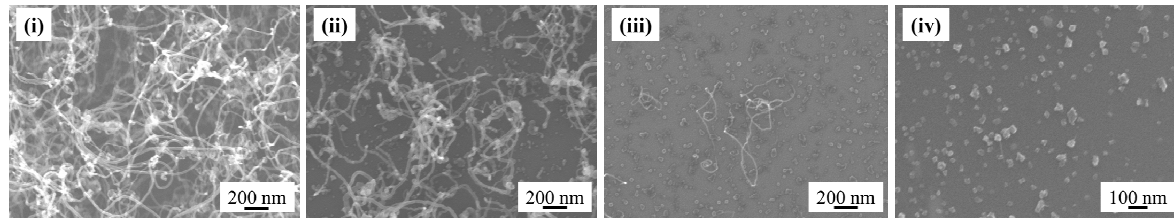


Figure 7. The surface morphology after the PECVD with different nanoparticle: (i) Fe (ii) $\text{Fe}_{0.5}\text{Mn}_{0.5}$ (iii) $\text{Fe}_{0.9}\text{Mn}_{0.1}$ (iv) Mn. The composition ratio is evaluated based on Vegard's law.

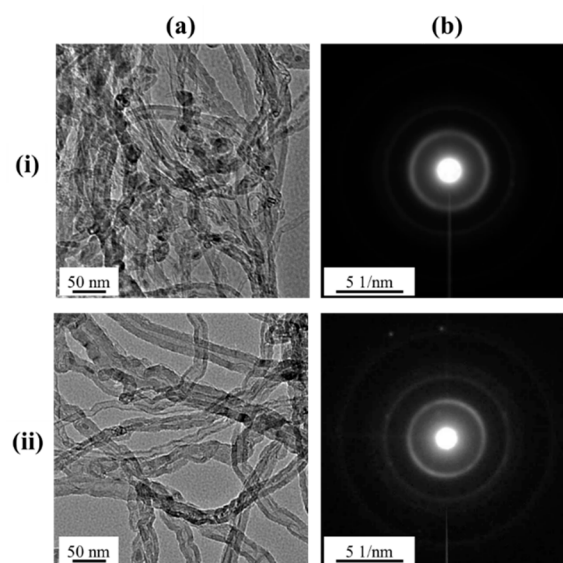


Figure 8. TEM images (a) and electron diffraction patterns (b) of CNTs grown with nanoparticles (i) and (ii).

Raman spectra of the samples (i) and (ii) were also obtained to elucidate the quality of CNTs as shown in Figure 9. The quality of CNTs can be evaluated by calculating the intensity ratio of D peak (I_D) and G peak (I_G) because the G band is assigned to the intrinsic vibrational mode of CNT, on the other hand, the D band is assigned to the defect mode [49,50]. I_D/I_G was calculated as 0.7 for sample (i) which is comparable to the reported value (0.2–0.7) of CNT with high quality [49,50] while I_D/I_G was calculated as 1.7 for sample (ii) which is much larger than that of the sample (i). A large I_D/I_G of the sample (ii) indicates the inclusion of the amorphous component. Fe in $\text{Fe}_{0.5}\text{Mn}_{0.5}\text{O}$ nanoparticles might not be mobile enough to make a nanotube with excellent crystallinity because the MnO is not reduced in the plasma environment and does not melt at this temperature (the melting point of the MnO is 1650°C). Lowering the catalytic activity of graphitization due to the inclusion of the MnO caused the formation of the amorphous component. Combining this result and the fact that the number density of CNT decreased as Mn component increased, we concluded that only high catalytic activity of graphitization was required to grow CNT in PECVD because high energy plasma decomposed the source gas. Raman of radius breathing modes (RBM) was also observed for the sample (i) at the region between $150\text{--}250\text{ cm}^{-1}$ as shown in the inset of Figure 9 while no RBM was seen for sample (ii). The RBM proved that the existence of the SWCNTs with a diameter of 1–2 nm. The formation of the SWCNTs is probably because FeO nanoparticles were the smallest among four kinds of nanoparticles;

hence, there was a chance to grow SWCNTs. On the other hand, SWCNT was not produced when using $\text{Fe}_{0.5}\text{Mn}_{0.5}\text{O}$ nanoparticles due to the large size.

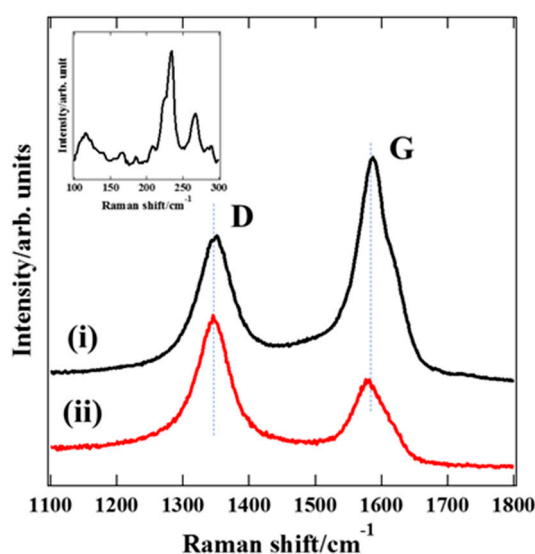


Figure 9. Raman spectra of the CNTs grown with (i) Fe nanoparticles and (ii) $\text{Fe}_{0.5}\text{Mn}_{0.5}$ nanoparticles. Inset shows the RBM of (i) in the range of 100–300 cm^{-1} .

4. Conclusions

We studied how the catalytic activity of graphitization influences the growth of CNT using $\text{Fe}_{1-x}\text{Mn}_x\text{O}$ nanoparticles as catalysts in PECVD. The number density of CNT decreases as the ratio of Mn increases, which shows that the catalytic activity can be tuned by controlling the composition ratio. Our results show that only the catalytic function of graphitization affects the yield and quality of CNTs. Although Fe or Ni is recognized as one of the best catalysts in PECVD, the decomposition function Fe or Ni possesses is not actually needed. We believe that our study will encourage researchers to search for a new catalyst with the high catalytic activity of graphitization, which is not necessary to show the catalytic activity of decomposition of a source gas.

Author Contributions: T.Y., T.M., T.S. (Tatsuya Shiratori) and M.W. conducted research and performing the experiments to obtain data/evidence. T.Y. and T.N. essentially contributed in discussion and in preparing the manuscript. T.S. (Toshihiro Shimada) planned the research, acquired the financial support for the project and reviewed the manuscript.

Funding: This work is partly supported by KAKENHI 17H03380, MEXT JAPAN.

Acknowledgments: Instrumental analysis was supported by the Nanotechnology Platform at Hokkaido University by METI, Japan.

Conflicts of Interest: The authors declare no conflict of interest.

References

1. Iijima, S.; Ichihashi, T. Single-shell carbon nanotubes of 1-nm diameter. *Nature* **1993**, *363*, 603–605. [[CrossRef](#)]
2. Iijima, S. Helical microtubules of graphitic carbon. *Nature* **1991**, *354*, 56–58. [[CrossRef](#)]
3. Hone, J.; Llaguno, M.; Biercuk, M.; Johnson, A.; Batlogg, B.; Benes, Z.; Fischer, J. Thermal properties of carbon nanotubes and nanotube-based materials. *Appl. Phys. A* **2002**, *74*, 339–343. [[CrossRef](#)]
4. Wong, E.; Sheehan, P.; Lieber, C. Nanobeam Mechanics: Elasticity, Strength, and Toughness of Nanorods and Nanotubes. *Science* **1997**, *277*, 1971–1975. [[CrossRef](#)]
5. Franklin, A. Electronics: The road to carbon nanotube transistors. *Nature* **2013**, *498*, 443–444. [[CrossRef](#)] [[PubMed](#)]
6. Tans, S.; Verschueren, A.; Dekker, C. Room-temperature transistor based on a single carbon nanotube. *Nature* **1998**, *393*, 49–52. [[CrossRef](#)]

7. Martel, R.; Schmidt, T.; Shea, H.; Hertel, T.; Avouris, P. Single-and multi-wall carbon nanotube field-effect transistors. *Appl. Phys. Lett.* **1998**, *73*, 2447–2449. [[CrossRef](#)]
8. Zhong, G.; Iwasaki, T.; Honda, K.; Furukawa, Y.; Ohdomari, I.; Kawarada, H. Low Temperature Synthesis of Extremely Dense and Vertically Aligned Single-Walled Carbon Nanotubes. *Jpn. J. Appl. Phys.* **2005**, *44*, 1558–1561. [[CrossRef](#)]
9. Nakai, Y.; Honda, K.; Yanagi, K.; Kataura, H.; Kato, T.; Yamamoto, T.; Maniwa, Y. Giant Seebeck coefficient in semiconducting single-wall carbon nanotube film. *Appl. Phys. Express* **2014**, *7*, 025103. [[CrossRef](#)]
10. Ebbesen, T.; Ajayan, P. Large-scale synthesis of carbon nanotubes. *Nature* **1992**, *358*, 220–222. [[CrossRef](#)]
11. Ando, Y.; Iijima, S. Preparation of Carbon Nanotubes by Arc-Discharge Evaporation. *Jpn. J. Appl. Phys.* **1993**, *32*, L107–L109. [[CrossRef](#)]
12. Thess, A.; Lee, R.; Nikolaev, P.; Dai, H.; Petit, P.; Robert, J.; Xu, C.; Lee, Y.; Kim, S.; Rinzler, A.; et al. Crystalline Ropes of Metallic Carbon Nanotubes. *Science* **1996**, *273*, 483–487. [[CrossRef](#)] [[PubMed](#)]
13. Dai, H.; Rinzler, A.; Nikolaev, P.; Thess, A.; Colbert, D.; Smalley, R. Single-wall nanotubes produced by metal-catalyzed disproportionation of carbon monoxide. *Chem. Phys. Lett.* **1996**, *260*, 471–475. [[CrossRef](#)]
14. Bachilo, S.M.; Balzano, L.; Herrera, J.; Pompeo, F.; Resasco, D.; Weisman, B. Narrow (n, m)-Distribution of Single-Walled Carbon Nanotubes Grown Using a Solid Supported Catalyst. *J. Am. Chem. Soc.* **2003**, *125*, 11186–11187. [[CrossRef](#)] [[PubMed](#)]
15. Li, X.; Tu, X.; Zaric, S.; Welsher, K.; Seo, W.; Zhao, W.; Dai, H. Selective synthesis combined with chemical separation of single-walled carbon nanotubes for chirality selection. *J. Am. Chem. Soc.* **2007**, *129*, 15770–15771. [[CrossRef](#)] [[PubMed](#)]
16. Takagi, D.; Homma, Y.; Hibino, H.; Suzuki, S.; Kobayashi, Y. Single-walled carbon nanotube growth from highly activated metal nanoparticles. *Nano Lett.* **2006**, *6*, 2642–2645. [[CrossRef](#)] [[PubMed](#)]
17. Ding, L.; Zhou, W.; Chu, H.; Jin, Z.; Zhang, Y.; Li, Y. Direct preparation and patterning of iron oxide nanoparticles via microcontact printing on silicon wafers for the growth of single-walled carbon nanotubes. *Chem. Mater.* **2006**, *18*, 4109–4114. [[CrossRef](#)]
18. Yuan, D.; Ding, L.; Chu, H.; Feng, Y.; McNicholas, T.P.; Liu, J. Horizontally aligned single-walled carbon nanotube on quartz from a large variety of metal catalysts. *Nano Lett.* **2008**, *8*, 2576–2579. [[CrossRef](#)]
19. Liu, B.; Ren, W.; Gao, L.; Li, S.; Liu, Q.; Jiang, C.; Cheng, H.M. Manganese-catalyzed surface growth of single-walled carbon nanotubes with high efficiency. *J. Phys. Chem. C* **2008**, *112*, 19231–19235. [[CrossRef](#)]
20. Takagi, D.; Kobayashi, Y.; Hibino, H.; Suzuki, S.; Homma, Y. Mechanism of gold-catalyzed carbon material growth. *Nano Lett.* **2008**, *8*, 832–835. [[CrossRef](#)]
21. Helveg, S.; López-Cartes, C.; Sehested, J.; Hansen, P.H.; Clausen, B.S.; Rostrup-Nielsen, J.R.; Abild-Pedersen, F.; Nørskov, J.K. Atomic-scale imaging of carbon nanofibre growth. *Nature* **2004**, *427*, 426–429. [[CrossRef](#)] [[PubMed](#)]
22. Nikolaev, P.; Bronikowski, M.; Bradley, R.; Rohmund, F.; Colbert, D.; Smith, K.; Smalley, R. Gas-phase catalytic growth of single-walled carbon nanotubes from carbon monoxide. *Chem. Phys. Lett.* **1999**, *313*, 91–97. [[CrossRef](#)]
23. Hata, H.; Futaba, D.; Mizuno, K.; Namai, T.; Yumura, M.; Iijima, S. Water-Assisted Highly Efficient Synthesis of Impurity-Free Single-Walled Carbon Nanotubes. *Science* **2004**, *306*, 1362–1364. [[CrossRef](#)] [[PubMed](#)]
24. Kitiyanan, B.; Alvarez, W.; Harwell, J.; Resasco, D. Controlled production of single-wall carbon nanotubes by catalytic decomposition of CO on bimetallic Co–Mo catalysts. *Chem. Phys. Lett.* **2000**, *317*, 497–503. [[CrossRef](#)]
25. Sanchez-Valencia, J.; Dienel, T.; Groning, O.; Shorubalko, I.; Mueller, A.; Jansen, M.; Amsharov, K.; Ruffieux, P.; Fasel, R. Controlled synthesis of single-chirality carbon nanotubes. *Nature* **2014**, *512*, 61–64. [[CrossRef](#)] [[PubMed](#)]
26. Yang, F.; Wang, X.; Zhang, D.; Yang, J.; Luo, D.; Xu, Z.; Wei, J.; Wang, J.; Xu, Z.; Peng, F.; et al. Chirality-specific growth of single-walled carbon nanotubes on solid alloy catalysts. *Nature* **2014**, *510*, 522–524. [[CrossRef](#)] [[PubMed](#)]
27. Hofmann, S.; Sharma, R.; Ducati, C.; Du, G.; Mattevi, C.; Cepek, C.; Cantoro, M.; Pisana, S.; Parvez, A.; Cervantes-Sodi, F.; et al. In situ Observations of Catalyst Dynamics during Surface-Bound Carbon Nanotube Nucleation. *Nano Lett.* **2007**, *7*, 602–608. [[CrossRef](#)] [[PubMed](#)]
28. Hongo, H.; Yudasaka, M.; Ichihashi, T.; Nihey, F.; Iijima, S. Chemical vapor deposition of single-wall carbon nanotubes on iron-film-coated sapphire substrates. *Chem. Phys. Lett.* **2002**, *361*, 349–354. [[CrossRef](#)]

29. Kong, J.; Soh, H.; Cassell, A.; Quate, C.; Dai, H. Synthesis of individual single-walled carbon nanotubes on patterned silicon wafers. *Nature* **1998**, *395*, 878–881. [[CrossRef](#)]
30. Su, M.; Zheng, B.; Liu, J. A scalable CVD method for the synthesis of single-walled carbon nanotubes with high catalyst productivity. *Chem. Phys. Lett.* **2000**, *322*, 321–326. [[CrossRef](#)]
31. Ghorannevis, Z.; Kato, T.; Kaneko, T.; Hatakeyama, R. Growth of single-walled carbon nanotubes from nonmagnetic catalysts by plasma chemical vapor deposition. *Jpn. J. Appl. Phys.* **2010**, *49*, 02BA01. [[CrossRef](#)]
32. Kato, T.; Hatakeyama, R. Direct growth of short single-walled carbon nanotubes with narrow-chirality distribution by time-programmed plasma chemical vapor deposition. *ACS Nano* **2010**, *4*, 7395–7400. [[CrossRef](#)] [[PubMed](#)]
33. Meyyappan, M. A review of plasma enhanced chemical vapor deposition of carbon nanotubes. *J. Phys. D* **2009**, *42*, 213001. [[CrossRef](#)]
34. Abdi, Y.; Mohajerzadeh, S.; Koochshorkhi, J.; Robertson, M.D.; Andrei, C.M. A plasma enhanced chemical vapor deposition process to achieve branched carbon nanotubes. *Carbon* **2008**, *46*, 1611–1614. [[CrossRef](#)]
35. Hofmann, S.; Kleinsorge, B.; Ducati, C.; Ferrari, A.C.; Robertson, J. Low-temperature plasma enhanced chemical vapour deposition of carbon nanotubes. *Diam. Relat. Mater.* **2004**, *13*, 1171–1176. [[CrossRef](#)]
36. Cole, M.T.; Milne, W.I. Plasma Enhanced Chemical Vapour Deposition of Horizontally Aligned Carbon Nanotubes. *Materials* **2013**, *6*, 2262–2273. [[CrossRef](#)] [[PubMed](#)]
37. Hou, Y.; Xu, Z.; Sun, S. Controlled Synthesis and Chemical Conversions of FeO Nanoparticles. *Angew. Chem. Int. Ed.* **2007**, *119*, 6445–6448. [[CrossRef](#)]
38. Donegá, C.M.; Liljeroth, P.; Vanmaekelbergh, D. Physicochemical evaluation of the hot-injection method, a synthesis route for monodisperse nanocrystals. *Small* **2005**, *1*, 1152–1162. [[CrossRef](#)]
39. Peng, X.; Wickham, J.; Alivisatos, A. Kinetics of II-VI and III-V colloidal semiconductor nanocrystal growth: “Focusing” of size distributions. *J. Am. Chem. Soc.* **1998**, *120*, 5343–5344. [[CrossRef](#)]
40. Shimada, T.; Miura, T.; Xie, W.; Yanase, T.; Nagahama, T. A thermocouple-based remote temperature controller of an electrically-floated sample for plasma CVD of nanocarbons with bias voltage. *Measurement* **2017**, *102*, 244–248. [[CrossRef](#)]
41. Kern, W. The Evolution of Silicon Wafer Cleaning Technology. *J. Electrochem. Soc.* **1990**, *137*, 1887–1892. [[CrossRef](#)]
42. Zhong, G.; Iwasaki, T.; Robertson, J.; Kawarada, H. Growth Kinetics of 0.5 cm Vertically Aligned Single-Walled Carbon Nanotubes. *J. Phys. Chem. B* **2007**, *111*, 1907–1910. [[CrossRef](#)] [[PubMed](#)]
43. Esconjauregui, S.; Fouquet, M.; Bayer, B.; Eslava, S.; Khachadorian, S.; Hofmann, S.; Robertson, J. Manipulation of the catalyst-support interactions for inducing nanotube forest growth. *J. Appl. Phys.* **2011**, *109*, 044303. [[CrossRef](#)]
44. Shukrullah, S.; Mohamed, N.; Shaharun, M. Optimum temperature on structural growth of multiwalled carbon nanotubes with low activation energy. *Diam. Relat. Mater.* **2015**, *58*, 129–138. [[CrossRef](#)]
45. Hernadi, K. Catalytic synthesis of multiwall carbon nanotubes from methylacetylene. *Chem. Phys. Lett.* **2002**, *363*, 169–174. [[CrossRef](#)]
46. Panic, S.; Bajac, B.; Rakić, S.; Kónya, K.A.Z.; Boskovic, V.G. Molybdenum anchoring effect in Fe-Mo/MgO catalyst for multiwalled carbon nanotube synthesis. *React. Kinet. Mech. Catal.* **2017**, *122*, 775–791. [[CrossRef](#)]
47. Jeong, H.; Kim, K.; Jeong, S.; Park, M.; Yang, C.; Lee, Y. High-yield catalytic synthesis of thin multiwalled carbon nanotubes. *J. Phys. Chem. B* **2004**, *108*, 17695–17698. [[CrossRef](#)]
48. Mizutani, K.; Kohno, H. Multi-walled carbon nanotubes with rectangular or square cross-section. *Appl. Phys. Lett.* **2016**, *108*, 263112. [[CrossRef](#)]
49. DiLeo, R.; Landi, B.; Raffaele, R. Purity assessment of multiwalled carbon nanotubes by Raman spectroscopy. *J. Appl. Phys.* **2007**, *101*, 064307. [[CrossRef](#)]
50. Delhaes, P.; Couzi, M.; Trinquescoste, M.; Dentzer, J.; Hamidou, H.; Vix-Guterl, C. A comparison between Raman spectroscopy and surface characterizations of multiwall carbon nanotubes. *Carbon* **2006**, *44*, 3005–3013. [[CrossRef](#)]

